

A SYSTEMATIC SEARCH FOR X-RAY CAVITIES IN THE HOT GAS OF GALAXY GROUPS

RUOBING DONG,¹ JESPER RASMUSSEN,^{2,3} AND JOHN S. MULCHAEY²

Accepted by ApJ, 2010 February 9

ABSTRACT

We have performed a systematic search for X-ray cavities in the hot gas of 51 galaxy groups with *Chandra* archival data. The cavities are identified based on two methods: subtracting an elliptical β -model fitted to the X-ray surface brightness, and performing unsharp masking. 13 groups in the sample ($\sim 25\%$) are identified as clearly containing cavities, with another 13 systems showing tentative evidence for such structures. We find tight correlations between the radial and tangential radii of the cavities, and between their size and projected distance from the group center, in quantitative agreement with the case for more massive clusters. This suggests that similar physical processes are responsible for cavity evolution and disruption in systems covering a large range in total mass. We see no clear association between the detection of cavities and the current 1.4 GHz radio luminosity of the central brightest group galaxy, but there is a clear tendency for systems with a cool core to be more likely to harbor detectable cavities. To test the efficiency of the adopted cavity detection procedures, we employ a set of mock images designed to mimic typical *Chandra* data of our sample, and find that the model-fitting approach is generally more reliable than unsharp masking for recovering cavity properties. Finally, we find that the detectability of cavities is strongly influenced by a few factors, particularly the signal-to-noise ratio of the data, and that the real fraction of X-ray groups with prominent cavities could be substantially larger than the 25–50% suggested by our analysis.

Subject headings: galaxies: active — galaxies: clusters: general — X-rays: galaxies: clusters

1. INTRODUCTION

Feedback and heating from active galactic nuclei (AGN) is considered a prime candidate for solving the “cooling flow” problem (Fabian 1994) in the hot gas of galaxy clusters (Birzan et al. 2004; Dunn & Fabian 2006; Rafferty et al. 2006; McNamara & Nulsen 2007), groups, and giant elliptical galaxies (Jones et al. 2002; Machacek et al. 2006), although the details of this process are not yet fully understood. Recent observations using *Chandra* and *XMM-Newton* have produced a large increase in the detection of X-ray surface brightness depressions (“cavities” or “bubbles”) in many of these systems, interpreted as buoyantly rising bubbles created by AGN outbursts. Studies of such cavities in individual clusters, including Hydra A (McNamara et al. 2000), Perseus (Fabian et al. 2000), A2052 (Blanton et al. 2001), A2199 (Johnstone et al. 2002), and Centaurus (Sanders & Fabian 2002), indicate that the outburst energy required to inflate these cavities would be sufficient to balance cooling (Birzan et al. 2004; Rafferty et al. 2006), explain the lack of gas cooling below $T \approx 2$ keV in cluster cores (Peterson et al. 2001; Kaastra et al. 2004), and reproduce the bright end of the galaxy luminosity function (Benson et al. 2003; Bower et al. 2006; Croton et al. 2006; Sijacki & Springel 2006).

Detailed studies of larger samples of X-ray bright elliptical galaxies and their surrounding cavities has further elucidated the possible role of AGN feedback for the thermal and morphological properties of the hot gas in these

systems. Best et al. (2005, 2006) combined observed cavity properties and central radio powers of the systems in the Birzan et al. (2004) sample with the inferred fraction of radio-loud ellipticals in the Sloan Digital Sky Survey, to show that the time-averaged heating rate by radio AGN in massive ellipticals can generally balance the cooling rate of the hot gas surrounding these galaxies. Using a sample of X-ray luminous ellipticals with identified cavities, Allen et al. (2006) estimated AGN jet powers from cavity properties and showed that these correlate tightly with the anticipated Bondi accretion rate of the central supermassive black hole. Evidence that radio AGN may be able to affect their gaseous surroundings also in lower-mass ellipticals has been provided by Diehl & Statler (2008a), who demonstrated that the amount of asymmetry in the hot gas morphology of ellipticals correlates with the central radio AGN luminosity, even down to the lowest detectable radio powers in relatively X-ray faint galaxies.

These results all point to a close connection between central AGN radio outbursts and the creation of X-ray cavities in the surrounding gas. In terms of establishing the incidence and nature of such cavities, most work so far has focused on studying cavity properties and AGN interactions with the intracluster medium (ICM) within galaxy clusters (Birzan et al. 2004; Dunn & Fabian 2004; Dunn et al. 2005; Dunn & Fabian 2006; Rafferty et al. 2006; Sternberg et al. 2007; Birzan et al. 2008; Rafferty et al. 2008; Diehl et al. 2008). Results suggest that roughly 2/3 of X-ray bright cool-core clusters harbor detectable cavities (Dunn & Fabian 2006), and that these cavities appear to obey tight scaling relations between their size and projected clustercentric distance, offering a means of testing their nature and that of the inflating

¹ Department of Astrophysical Sciences, Princeton University, Princeton, NJ 08544, rdong@princeton.edu

² Observatories of Carnegie Institution of Washington, 813 Santa Barbara Street, Pasadena, CA 91101

³ Chandra Fellow

mechanism (Diehl et al. 2008). Comparable work on giant elliptical galaxies that do not represent central brightest cluster galaxies is so far limited (Allen et al. 2006; McNamara & Nulsen 2007), but indicates a significantly smaller detectable cavity fraction of $\sim 1/4$ (McNamara & Nulsen 2007). However, studies of AGN heating and X-ray cavities within large samples of galaxy groups have largely been absent. Although AGN outbursts in groups are assumed to be smaller in scale and less energetic than those in clusters, they may play a more prominent role in the evolution of the host structure due to the shallower gravitational potential of groups. Estimating the incidence and properties of X-ray cavities in groups is therefore an important step toward understanding the role played by AGN outbursts for the evolution of baryons on group scales.

In many X-ray bright clusters with high-quality data, X-ray cavities are prominent and can be easily identified as X-ray surface brightness depressions using visual inspection. This can be augmented by radio data revealing ongoing AGN activity within the central cluster galaxy, or the presence of radio lobes coincident with the cavities. In this process, a number of factors could affect the detectability of X-ray cavities however, including the position, orientation, and angular extent of the cavities (Enßlin & Heinz 2002; Diehl et al. 2008; Brüggén et al. 2009), along with observational details such as the sensitivity of the data. These issues are even more important in the group regime, where the lower intrinsic X-ray luminosities can further impede cavity identification. To search for X-ray cavities in groups, it is therefore important to consider additional methods that can aid simple visual inspection in identifying these structures.

In the present work, we select a sample of 51 galaxy groups from the *Chandra* archive, in order to systematically search for and characterize the presence of X-ray cavities in a large sample of galaxy groups. In addition to visual inspection of the raw X-ray data, we facilitate the detection process by employing two methods to first characterize the large-scale group emission, *viz.* unsharp masking and modeling of the surface brightness distribution. A good handful of the groups in our sample have been previously reported to harbor detectable cavities. Here we find that at least 13 of the groups, and potentially as much as half of our group sample (26/51), show evidence of X-ray cavities. We quantify the size, group-centric distance, and relationship with the central AGN radio luminosity for all these structures, in addition to offering some considerations as to the preferred method for identifying cavities in these relatively X-ray faint systems.

The structure of this paper is as follows. In Section 2 we present the group sample and outline the data reduction process. Our approach to searching for cavities and establishing their properties are described in detail in Section 3. Section 4 presents the results of our *Chandra* analysis. To understand the efficiency of the two methods employed for cavity detection, we generated a set of mock data sets, the analysis of which is described in Section 5. This is followed by a discussion of our results in Section 6 and conclusions in Section 7. The cosmological parameters assumed in this paper are $H_0 = 73 \text{ km s}^{-1} \text{ Mpc}^{-1}$, $\Omega_m = 0.27$, and $\Omega_\Lambda = 0.73$. Unless otherwise stated, all uncertainties are quoted at

the 68% confidence level.

2. SAMPLE SELECTION AND DATA REDUCTION

The groups in this study were selected from the *Chandra* archival samples of Sun et al. (2009) (43 groups) and Rasmussen & Ponman (2007) (an additional 9 groups). To suppress the potential impact of instrumental artifacts on our results, only groups for which the central bright regions are covered by a single ACIS CCD were considered. This excluded one group (A160) from the sample. Our final sample is listed in Table 1 and includes 51 groups, ranging in distance from ~ 20 –550 Mpc. A few of the groups have been covered by multiple *Chandra* observations. In those cases, we generally used the longest observation unless this had a large offset between the group center and the CCD aimpoint. We stress that the sample does not contain individual giant elliptical galaxies, nor any galaxy clusters, and that the two studies from which our sample is drawn were not themselves designed for cavity studies. Hence, while the selection criteria employed in those two studies favor fairly undisturbed X-ray bright systems, the sample should not be inherently biased toward systems with prominent cavities.

Standard data reduction and calibration was performed to all data sets starting from level one event files. *Chandra* Interactive Analysis of Observations software (CIAO) v.4.1.1 and *Chandra* Calibration Database (CALDB) 4.1.1 were used in this work. New level one event files were created with the “*acis_process_events*” task in CIAO, including charge transfer inefficiency correction, time-dependent gain adjustment, and screening for bad pixels using the bad pixel map provided by the pipeline. For observations taken in Very Faint mode, additional background screening was performed. Grade/status filters were applied (excluding *ASCA* grades 1, 5, and 7) along with Good Time Intervals filters to produce level two event files. Times of high background were eliminated based on lightcurves extracted in regions away from the extended source center. Images were then produced in the 0.3–2 keV band, chosen to optimize the signal-to-noise ratio at the typical group temperatures of our sample, using spatial bins of 1 or 2 pixels depending on source extent and data quality. Exposure maps were produced assuming a monoenergetic distribution of source photons at the peak flux energy (usually around 1 keV). The source image was normalized by the exposure map, correcting for the effect of strongly variable exposure near the detector edges. We adopt a threshold of 1.5% of the maximum value of the exposure map, setting all pixels with exposure below this value equal to zero.

3. DATA ANALYSIS

To search for small-scale X-ray structure and identify potential cavities, we employ two methods: Modeling the surface brightness distribution of the groups using a two-dimensional (elliptical) β -model and performing an unsharp masking procedure.

3.1. Elliptical β -Model Fitting

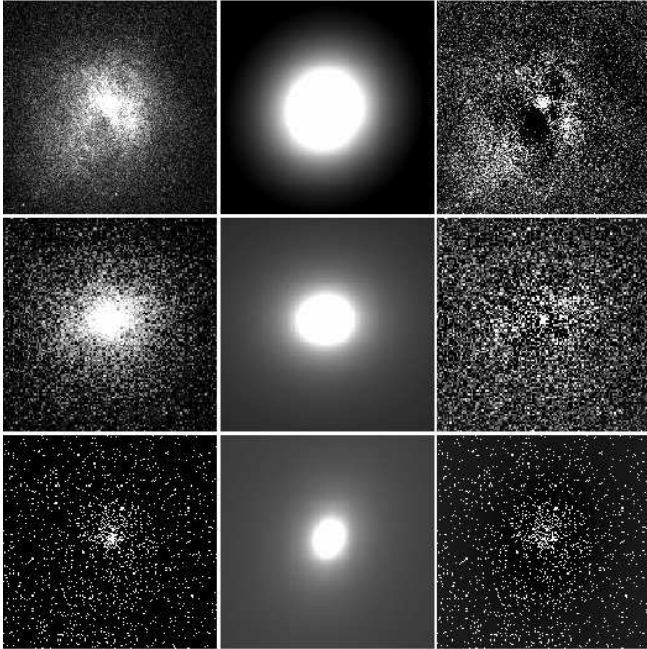


FIG. 1.— Illustration of elliptical β -model fitting results for NGC 5044 (top row), NGC 3402 (middle row) and ESO 552-020 (bottom). From left to right: Input source image, fitted model, and residual image.

With this method, we first aim to characterize the large-scale group emission by means of an elliptical β -model (Cavaliere & Fusco-Femiano 1976). We use the Sherpa package in CIAO to fit this model along with a uniform background to the exposure-corrected 0.3–2 keV images of all groups. Bright point sources were identified visually and masked out in all fitting, and only data from the central CCD were considered. Free parameters of the model are β , r_c , ellipticity, position angle, and the normalization, in addition to the local background level.

For each group, the best-fit model was subtracted from the input image to produce a residual image. For a good fit, the residual image will be flat almost everywhere (modulo Poisson fluctuations), with any remaining structure revealing departures from the model, such as cavities. The top panel of Figure 1 shows an example of this, displaying the results for NGC 5044, the group with the largest number of source counts and the most prominent cavities within our sample. In this case, the two cavities are already visible in the original image but become much more prominent in the residual image. The middle panel of Figure 1 shows the case of NGC 3402, in which cavities are not clearly detected. Here the fitted model describes the group emission very well, and residual “structure” can be largely ascribed to Poisson fluctuations. Finally, images with low signal-to-noise ratio tend to have no cavities detected, as illustrated in the bottom panel of Figure 1. In this case, the relatively low number of counts precludes any robust conclusion regarding the presence of cavities.

For some groups the model fitting fails to converge on sensible parameters, returning, e.g., a best-fit core radius smaller than one pixel or a model eccentricity higher than 0.99. The relevant systems are 3C 442A, A1139, A1238, A1692, A1992, A2092, A2462, NGC 507,

RBS 461, RXJ 1206-0744, and UGC 842. We ascribe the failure of the fitting approach mainly to the fact that many of these data sets have relatively low signal-to-noise ratio, coupled with the possibility that some of those groups are simply not well described by an elliptical β -model. We will return to these issues in Section 5.

3.2. Unsharp Masking

Another way to smooth the large-scale group emission and test for structure on smaller scales is unsharp masking. This approach has been successfully employed to uncover faint features at fine spatial detail in deep cluster X-ray data (e.g., Fabian et al. 2006). Here we perform this procedure by smoothing the exposure-corrected images using the “aconvolve” task in CIAO. For each group, the data are first smoothed using a wide Gaussian kernel that preserves the overall morphology of the emission but erases small-scale structure. A separate smoothing is performed on smaller scales to suppress (partly noise-induced) pixel-to-pixel variations while preserving structure on the likely scale of any cavities in the data. The latter image is then divided by the former, with the resulting quotient image acting as an analog of the residual image from the model fitting approach. In principle, optimal choices for the characteristic smoothing scales vary among the groups. In practice, however, we found that large and small scales of 10–30 and 2–5 pixels, respectively, generally produced the most visually compelling results, with the smaller values generally preferred for more distant and compact systems. Figure 2 illustrates this method applied to NGC 5044. The Figure shows the original image, the image smoothed by narrow and wide Gaussians of $\sigma = 3$ and 30 pixels, respectively, and the result of dividing the former by the latter. The result can be directly compared to the residual image from model fitting shown in the top row in Figure 1.

To illustrate the impact of different choices for the small smoothing scale, Figure 3 shows the quotient image for NGC 5044 with six different small scales employed along with a fixed large-scale kernel of $\sigma = 30$ pixels. All the quotient images clearly reveal X-ray depressions at the positions of the cavities, but it is easier to visually recognize the cavities as such in the images produced with relatively narrow small-scale kernels: The cavities in these images are more obvious and have a higher contrast with their surroundings. On the other hand, when the small scale becomes larger than 8 pixels (i.e. $> 1/4$ of the larger scale), distinguishing the cavities from other brightness depressions becomes more difficult as the sharp contrast between the cavities and their immediate surroundings is lost. However, we emphasize that NGC 5044 is by far the highest-flux system in our sample, and that the choice of small smoothing scale is less straightforward for significantly fainter systems. As such, a major drawback of this method compared with surface brightness modeling is the need to make appropriate choices for the smoothing scales.

3.3. Cavity Identification and Characterization

Based on the images described in Sections 3.1 and 3.2, visual inspection for X-ray cavities was performed for all groups. Cavities were mainly identified in the residual images from model fitting, but the appearance of the unsmoothed exposure-corrected images was also taken into

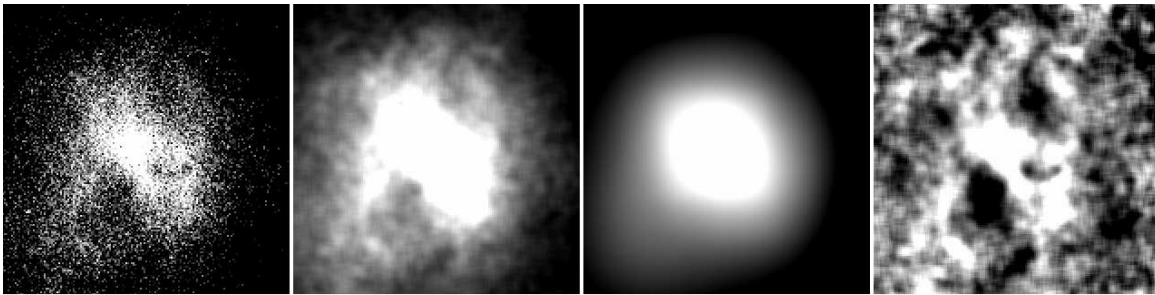


FIG. 2.— Illustration of unsharp masking for NGC 5044. From left to right: exposure-corrected image, small-scale smoothed image (Gaussian of $\sigma = 3$ pixels), large-scale smoothed image ($\sigma = 30$ pixels), and quotient image.

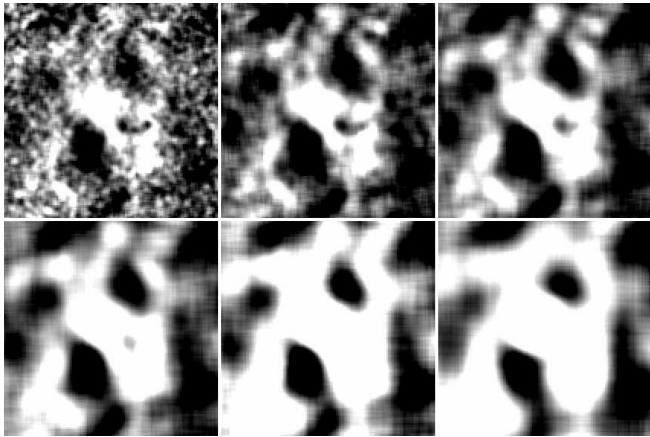


FIG. 3.— The effect of choosing different widths of the small-scale Gaussian kernel in unsharp masking for NGC 5044. From left to right, top to bottom: quotient images with $\sigma = 2, 4, 6, 8, 10,$ and 15 pixels (the large-scale kernel has $\sigma = 30$ pixels).

consideration. In most cases the impression gained from these two images agree. In the cases for which the fitting approach did not converge on reasonable model values (typically for sources of low signal-to-noise ratio), cavities were identified visually based on the raw images, aided by the quotient images from unsharp masking. For the groups judged to show evidence of cavities, differences in signal-to-noise ratio and in the contrast between the cavities and their surroundings led us to further subdivide the sample, leading to the following classification scheme:

Groups with certain cavities (denoted the “C”-sample in the following): Cavities are clearly detected upon visual inspection of the residual images, and their presence is at least indicative in the raw and unsharp masked images as well. These cavities always present a high contrast with their surroundings, including the presence of a bright rim.

Groups with possible cavities (“P”-sample), fulfilling one of two conditions: (1) Cavities are apparent in only one of the residual and raw images. (2) Both the residual image and the raw image show a hint, if not conclusive, of the presence of cavities. Cavities in this category always have a low contrast with their surroundings.

Groups with no cavities (“N”-sample): Neither raw nor residual images show any visually obvious evidence of cavities. This category also includes cases in which the surface brightness depression in the residual image

forms a ring around the group center. This is likely an artifact of the fitting procedure, owing to the presence of a strong central and extended excess above the best-fit β -model.

We emphasize that cavity detection was done solely on the basis of X-ray data, and that the presence or morphology of central radio emission in a group was not considered for this purpose. Furthermore, as indicated by comparison with other existing studies (see Section 4), we have likely been conservative in our classification. It is, therefore, conceivable that groups in the P-sample may generally have a high probability of containing cavities.

In addition to identifying cavities we also provide quantitative estimates of their properties. In each case, the cavity center was first defined as the centroid of the X-ray surface brightness depression. In a few cases where the deepest depression point of the cavity in the residual image from model fitting differed significantly from the apparent geometrical center, we considered the cavity center to be the midpoint between the two locations. The location of cavity boundaries were identified as sharp drops in X-ray surface brightness, equivalent to where the pixel counts in the residual images become negative. On this basis, the cavities can be generally viewed as ellipses, with a major axis a in the tangential direction (perpendicular to the line joining the cavity with the group center) and a minor axis b in the radial direction. The cavity distance D was defined as the distance between the cavity center and the group center, with the latter defined as the location of the central peak of the extended X-ray emission. Since the accuracy of these somewhat subjective measurements generally depends in an unquantifiable manner on factors such as the signal-to-noise ratio of the data, we do not provide uncertainties on these results, and we stress that they should all be considered approximate. We do note, however, that the inferred properties of the cavities in the P-sample are generally more uncertain than those of the C-sample.

4. RESULTS

Based on the above criteria, 26 out of the 51 groups in our sample were identified as harboring certain or possible X-ray cavities. These systems are evenly split among the C- and P-samples. In Figure 4 we show the input image, the residual image from model fitting, and the quotient image from unsharp masking for all groups in the C-sample. Figure 5 shows the corresponding results for the P-sample. For further comparison, we also show

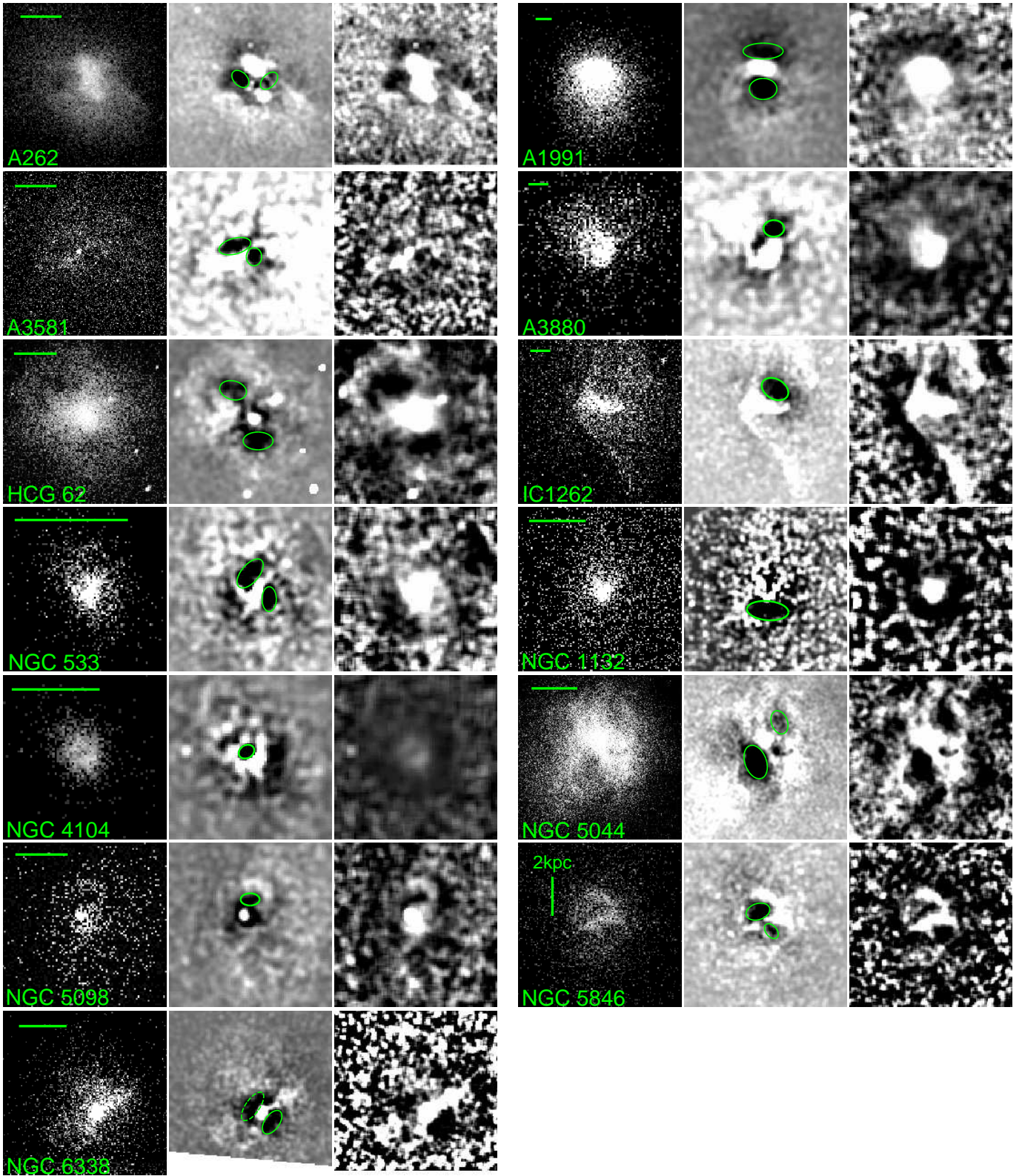


FIG. 4.— The 13 groups in the C-sample with clearly identified cavities. For each group, left panel shows the exposure-corrected image, middle panel the residual image from model fitting smoothed by a Gaussian of $\sigma = 2$ or 3 pixels, and right panel the quotient image from unsharp masking. Ellipses overlaid on the residual images outline identified cavities. Horizontal bars mark a physical scale of 10 kpc. Where appropriate, vertical bars are used to indicate a different scale.

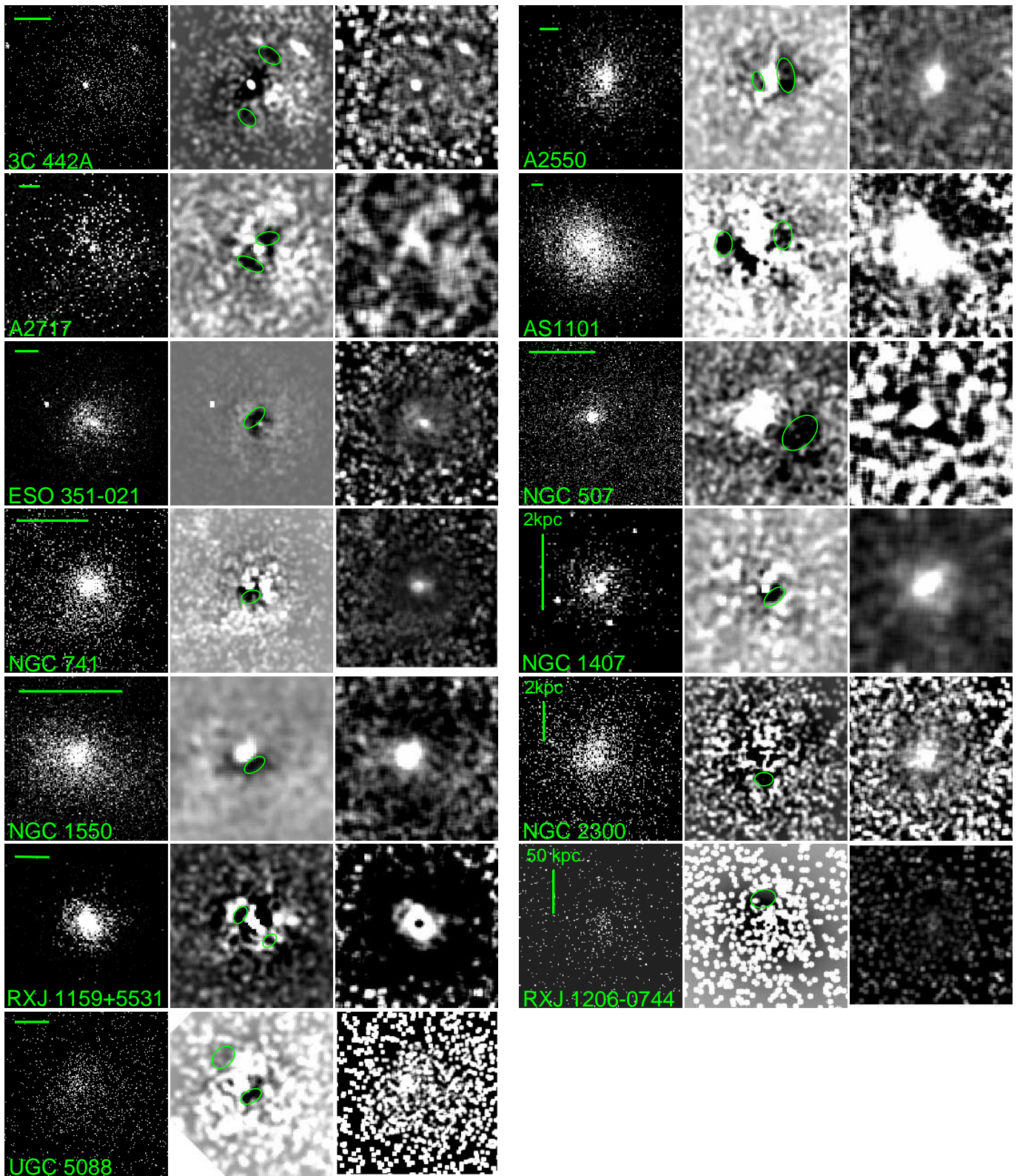


FIG. 5.— As Figure 4, but for the 13 groups in the P-sample with tentative evidence of cavities.

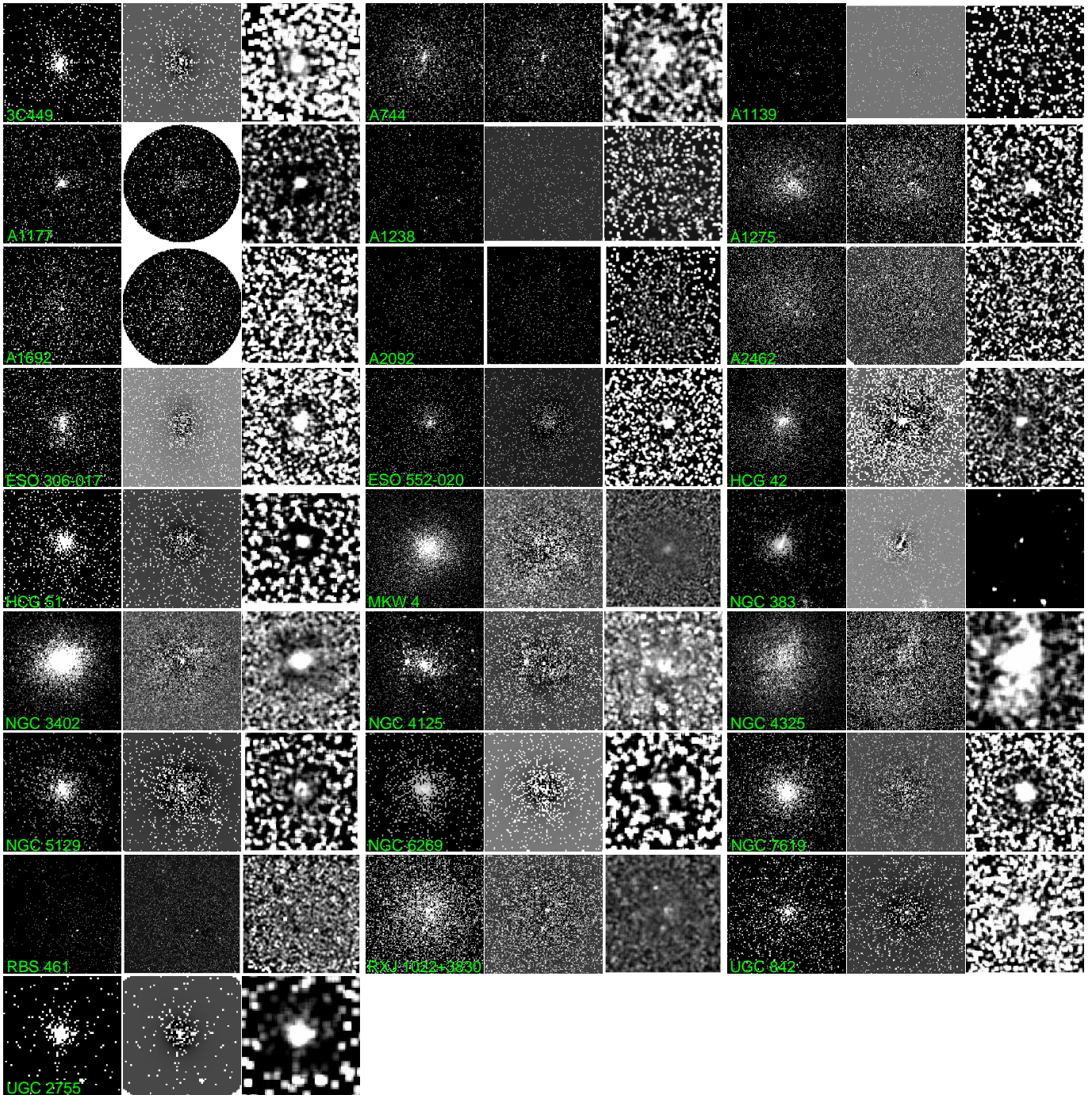


FIG. 6.— As Figure 4, but for the 25 groups in the N-sample without clearly identifiable cavities. The residual images in this figure have not been smoothed.

the images for the N- sample in Figure 6.

Among the 26 groups in the combined C- and P-samples, about half (8 in the C- sample and 6 in the P- sample) show evidence of containing two cavities, and these are always at symmetric positions relative to the group center. We did not identify any groups showing evidence for more than two cavities as otherwise reported for a number of galaxy clusters (e.g., Sanders & Fabian 2007; Wise et al. 2007). At least nine groups in our sample have been identified in previous work as hosting cavities: IC 1262 (Trinchieri et al.

2007), A262 (Birzan et al. 2004), HCG 62 (Morita et al. 2006), NGC 507 (Kraft et al. 2004; Allen et al. 2006), NGC 5846 (Allen et al. 2006), NGC 741 (Jetha et al. 2007), NGC 4325 (Russell et al. 2007), NGC 5044 (Gastaldello et al. 2009), and NGC 5098 (Randall et al. 2009). Eight of these were classified as belonging to the C- or P-sample in our analysis. The only exception is NGC 4325, which shows weak hints of the presence of cavities but without satisfying our criteria for inclusion in the P-sample. The identification of cavities in this system by Russell et al. (2007) was based on a detailed

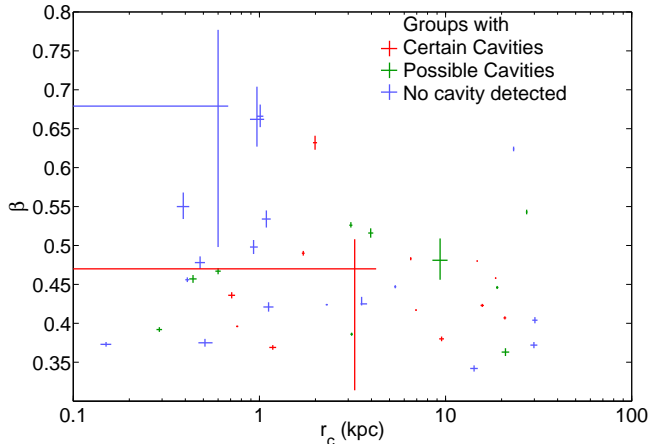


FIG. 7.— Fitted β -values and core radii with 1σ error bars for the C-sample (red), P-sample (green), and N-sample (blue).

Bayesian model-fitting approach which clearly exceeds the level of sophistication employed in our analysis. Furthermore, two of the above nine groups (NGC 507 and NGC 741) were here classified as belonging to the P- rather than C-sample. These comparisons confirm our suspicion that we have been fairly conservative in our classification. This might be anticipated given that we are not incorporating, e.g., radio data to aid in cavity identification.

We list the β -model fit results and cavity measurements (where applicable) for all the groups in Table 2, along with the total number of exposure-corrected 0.3–2 keV photons from diffuse emission within the model fitting region considered for each group (typically the central $\sim 5' \times 5'$). In agreement with many previous studies (e.g., Osmond & Ponman 2004), we note that the mean β -value derived for the sample is $\beta = 0.47$, considerably lower than the typical value of $\beta \approx 2/3$ seen in clusters (Arnaud & Evrard 1999; Mohr et al. 1999). We also tested for a relationship between β and core radius r_c for all three subsamples of groups, as illustrated in Figure 7. No clear correlation between these two parameters is evident, neither for the individual subsamples nor for all groups combined. In addition, mean values of the two parameters do not show any clear variation among the subsamples, being ($r_c = 7.9$ kpc, $\beta = 0.45$) for the C-sample, ($r_c = 8.8$ kpc, $\beta = 0.46$) for the P-sample, and ($r_c = 6.5$ kpc, $\beta = 0.49$) for the N-sample.

From the results in Table 2, we can explore any correlations among the sizes and groupcentric distances of the identified cavities. Figure 8(a) shows the relationship between the cavity size in the tangential direction a and radial direction b for the C- and P-samples. Remarkably, these two quantities appear strongly coupled, despite the potentially considerable systematic uncertainties associated with their estimation. Motivated by the appearance of the data in Figure 8, we fitted linear relations to the data in log–log space to quantify the observed cavity behavior. For this, we used the orthogonal regression approach of Isobe et al. (1990), since there are (unquantifiable) errors on both parameters, but we note that results are consistent with those obtained using various ordinary

least squares methods (e.g., Y vs. X , X vs. Y , bisector). For the data in Figure 8(a), we then find

$$\log a = (1.00 \pm 0.03) \log b + (0.22 \pm 0.02), \quad (1)$$

for a and b in kpc and with a high correlation coefficient of 0.95. This shows that cavities maintain broadly similar shapes, with a mean ratio of $a/b \approx 1.7$ that is roughly constant for all cavity sizes. Cavity sizes are also strongly correlated with their projected distance D from the group center. Figure 8(b) and (c) show a and b as functions of D (also in kpc), with best-fit linear relationships of

$$\log a = (0.86 \pm 0.04) \log D + (0.20 \pm 0.03), \quad (2)$$

for a correlation coefficient $r = 0.94$, and

$$\log b = (0.87 \pm 0.03) \log D - (0.03 \pm 0.02), \quad (3)$$

for a coefficient $r = 0.88$. As illustrated by the dotted line in Figure 8(b), equation (2) implies that cavities are enclosed by a cone of roughly constant opening angle $\theta \sim 60^\circ$ as they rise and expand within the surrounding medium.

In Figure 8, the fits of equations (1)–(3) are represented by solid lines. For comparison, we also show by dashed lines our corresponding fits to the results for the cluster sample of Birzan et al. (2004; their table 3), namely

$$\begin{aligned} \log a &= (1.07 \pm 0.07) \log b + (0.10 \pm 0.07), \\ \log a &= (0.92 \pm 0.07) \log D + (0.13 \pm 0.07), \\ \log b &= (0.85 \pm 0.06) \log D + (0.04 \pm 0.06). \end{aligned}$$

In addition, Figure 8(b) further shows the relation between a and D found by Diehl et al. (2008) for an even larger cluster sample. Despite the somewhat subjective way cavity sizes are estimated by different authors, there is generally remarkable agreement between these three studies and hence between results for our groups and more massive clusters. In particular, the slopes of equations (1)–(3), along with two out of three intercepts, are statistically consistent at the $1\text{-}\sigma$ level with the results of Birzan et al. (2004).

We next tested for a correlation between the 1.4 GHz radio luminosity $L_{1.4\text{GHz}}$ of the central brightest group galaxy (i.e., that of any central radio source associated with the galaxy itself rather than that of any radio lobes coinciding with the X-ray cavities) and the detection of cavities. Values of $L_{1.4\text{GHz}}$ were extracted from the NRAO VLA Sky Survey (NVSS), and are listed in Table 2. If data were missing at 1.4 GHz but available at a nearby frequency, we extrapolated to 1.4 GHz assuming a power-law spectrum of index unity, $S \propto \nu^{-1}$. For groups with NVSS coverage but with no radio flux listed in NED, we used the 99% completeness flux limit in the NVSS survey (3.4 mJy; Condon et al. 1998) to estimate an upper limit to $L_{1.4\text{GHz}}$. Finally, if a source was not covered in NVSS or if the 1.4 GHz emission could not be unambiguously associated with the central group galaxy in NVSS or FIRST (Becker et al. 1995) data, we left $L_{1.4\text{GHz}}$ as undetermined.

Figure 9 shows the resulting distribution of $L_{1.4\text{GHz}}$ for the different group subsamples. For groups with upper limits to $L_{1.4\text{GHz}}$, we have assumed this upper limit when displaying these results, but we note that the results would not be substantially affected by excluding

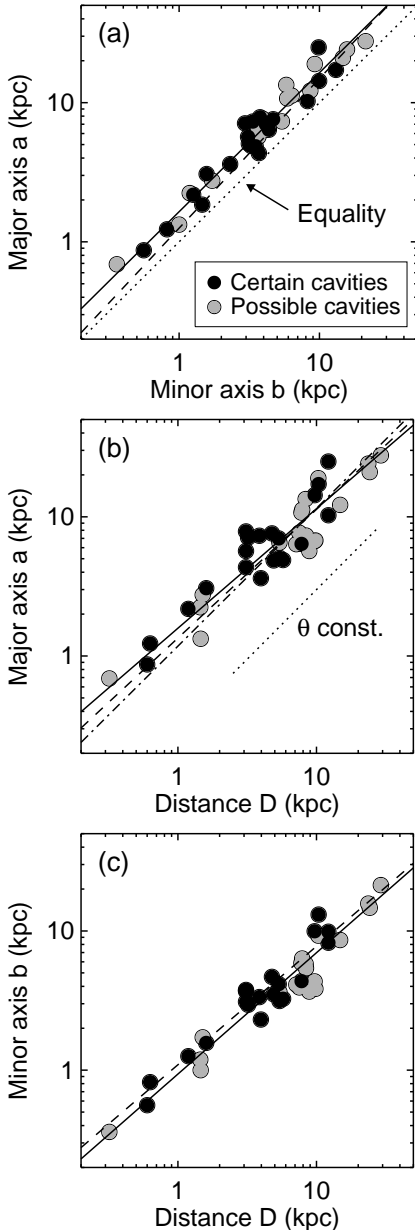


FIG. 8.— (a) Cavity major axis a as a function of minor axis b for the C- and P-samples. Dotted line represents equality. (b) Major axis as a function of projected cavity groupcentric distance D . Dotted line illustrates the (arbitrarily normalized) expectation for cavities enclosed by a cone of constant opening angle θ , and dot-dashed line shows the fitted relation of Diehl et al. (2008). (c) Minor axis as a function of D . Solid lines in all plots show the best-fit linear relations for our group sample, equations (1)–(3), while dashed lines represent our fits to the cluster results of Birzan et al. (2004).

those groups. There is no strong link between the presence of detectable cavities and the current radio power of the central group galaxy. For example, the geometric mean of $L_{1.4\text{GHz}}$ is very similar for the three subsamples, $10^{22.44} \text{ W Hz}^{-1}$ (C-sample), $10^{22.58} \text{ W Hz}^{-1}$ (P), and $10^{22.49} \text{ W Hz}^{-1}$ (N). Again, excluding groups with upper limits to $L_{1.4\text{GHz}}$ does not change this conclusion. We also note that no strong trend is seen between projected cavity distance D and $L_{1.4\text{GHz}}$, with the data showing a

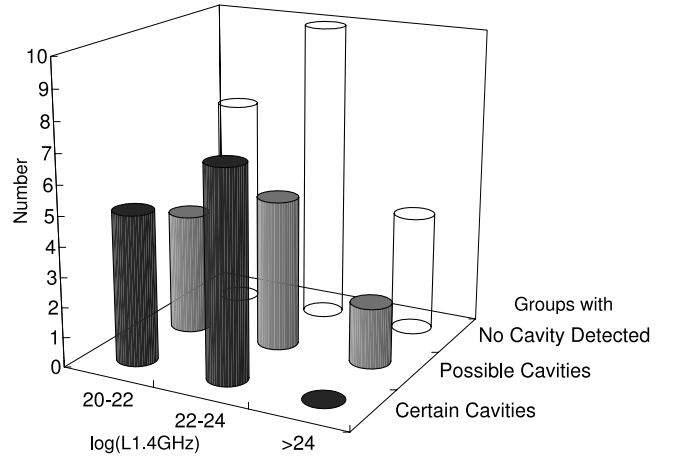


FIG. 9.— Distribution of central 1.4 GHz radio luminosities for the different subsamples.

small correlation coefficient of 0.4.

Finally, to search for evidence of a 1.4 GHz radio plasma at the location of the cavities, we have compared the X-ray and radio morphology of the groups in the C- and P-samples, using radio data extracted from NVSS and FIRST. Since the cavities are generally present on spatial scales well below the resolution of NVSS data, comparison between *Chandra* and NVSS data generally provides no clear evidence of any morphological similarities. However, 12 of our groups have higher-resolution FIRST data in NED, and of those 12 systems, we show the six groups belonging to the C- or P-samples in Figure 10. No clear association between the X-ray cavities and any radio lobes is seen, however. It remains a possibility that the cavities coincide with radio emission at frequencies well below 1.4 GHz (e.g., Giacintucci et al. 2009).

5. TESTING CAVITY DETECTION WITH MOCK DATA

To test the performance of the adopted methods for cavity detection and better understand the biases inherent in either method, we next generated a set of mock images designed to match typical *Chandra* exposures within our sample. These images were then analyzed in a manner similar to that of the real data. This Section describes the generation and analysis of these mock data.

5.1. Model Setup

The mock images were generated by first modeling the group emission as an elliptical β -model. Cavities were superposed as circular depressions in local surface brightness, and a spatially uniform background was added. The following sets of model parameters were considered:

- $\beta = \{0.35, 0.50, 0.65\}$.
- Core radius $r_c = 10$ pixels.
- Total number of source counts $N_{\text{tot}} = \{5,000, 15,000, 30,000\}$.
- Cavity “strength” (the local surface brightness depression factor): $\{1.5, 2.0, 2.5\}$.

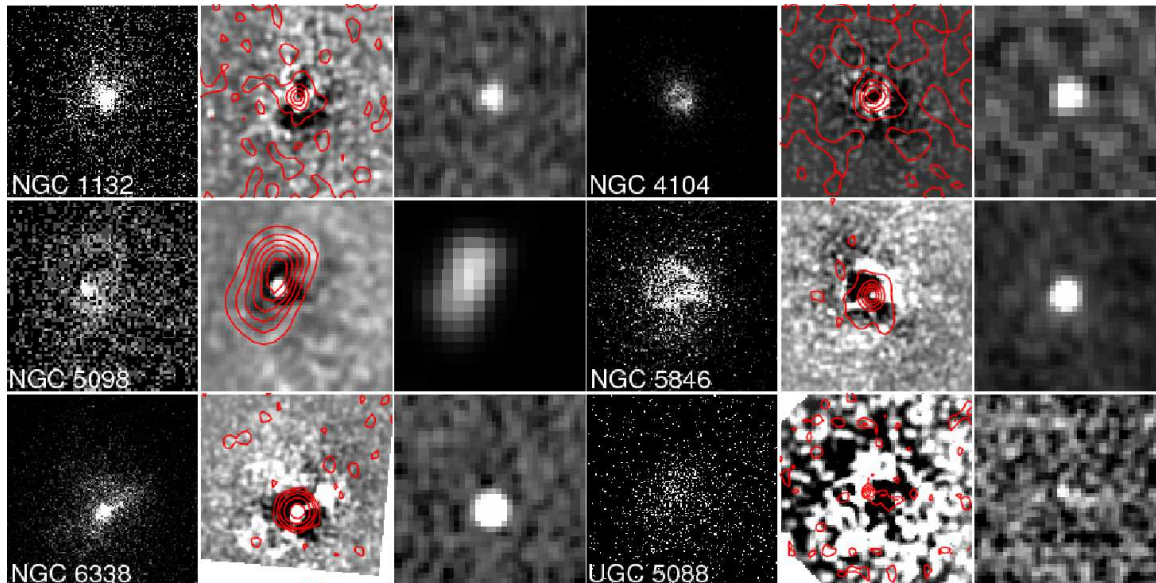


FIG. 10.— Comparison of X-ray and radio morphology for the 6 groups in the C- and P-samples with available FIRST radio data. For each group, left panel shows the exposure-corrected image, center panel the residual image, and right panel the FIRST 1.4 GHz image. Contours extracted from the radio data have been overlaid on the residual images. The first five groups belong to the C-sample, while UGC 5088 belongs to the P-sample.

- Projected cavity distance D from X-ray peak in pixels: {15, 35}.

This choice of parameters was generally motivated by the results for our real sample. The adopted β -values span the range of fitted values covered by all but four of our groups. To keep the number of output images at reasonable levels, r_c was fixed for all mock data. This should not introduce any substantial systematic bias in the results, since Figure 7 shows that r_c does not vary systematically with β for our groups. Values of N_{tot} were chosen to range from the median of the groups with no detected cavities (~ 5000) to a value below that of HCG 62, one of the groups with the most prominent and obvious cavities. For the cavity radii, we assumed $R = 0.6D$, in rough agreement with equation (2).

A total of 54 mock images were generated to span all combinations of the above parameters. For each image, a uniform background level was added, drawn from a Gaussian distribution with a mean equal to the approximate 0.3–2 keV value for a typical 50-ks ACIS-S exposure (≈ 0.1 counts arcsec $^{-2}$), and with $\sigma = 0.2 \times \text{mean}$. The minor-to-major axis ratio of the β -model was drawn from a Gaussian with mean 0.8 and $\sigma = 0.12$ (Mohr et al. 1995), but was restricted to ≥ 0.65 . Position angles of the β -model and of the cavities themselves were independently drawn randomly from a uniform distribution. The resulting surface brightness model was then convolved with the *Chandra* point spread function, derived using the “mkpsf” tool in CIAO at a photon energy of 1 keV and at the detector position of the ACIS-S3 aimpoint. Finally, Poisson noise was added to the mock images. Other instrumental effects (or point sources) were not included, since the model fitting to the real data was performed on exposure-corrected and point-source excised images.

Admittedly, the model setup is a rather simplistic one; we assume the number of cavities in each system is al-

ways two, they represent similar (local) brightness depressions, appear circular, and are at the same distances from the center of the X-ray emission. As such, orientation effects were not taken into account (e.g., the cavities were assumed to be in the plane of the sky). However, since the purpose of this exercise was simply to test and understand our ability to recover cavities in the real data under reasonably favorable conditions, a detailed exploration of the full cavity parameter space would be beyond the scope of this work.

5.2. Cavity Detectability

We applied both the methods described in Section 3 to the mock images in a test of the veracity of either approach. Figure 11 shows two example mock images, with $N_{\text{tot}} = 30,000$ and 5,000, respectively, along with the results of our two methods. For the brighter source, the input cavities are easily recognizable in both output images. For the fainter case, however, there is some ambiguity as to the apparent location of cavities in the two output images. We will return to this issue below. Figure 12 shows the distributions of best-fit values of core radius and β obtained from surface brightness modeling of all the mock images. Encouragingly, all distributions are peaked at the input values, lending credibility to the use of this method for describing group emission on large scales. For example, even though the mock sources are, on average, fainter than our real ones, there is no overlap between the resulting distributions for the three input values of β . Figure 13 summarizes the results of searching for cavities in both the output mock images, the quotient images, and the residual images. While the rate of “certain” cavity recovery is comparable for the unprocessed and quotient images, using the residual images is clearly more efficient, with the success rate increasing by a factor of two (from 14–17 to 30 out of the 54 data sets).

We found that all four controllable input parameters

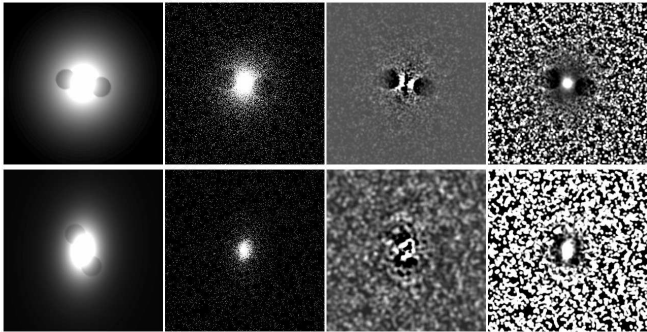


FIG. 11.— Two examples of raw and processed mock images: Top panel shows a model with total source counts $N_{\text{tot}} = 30,000$, $\beta = 0.65$, cavity strength 2.5 (prominent cavities) and cavity distance $D = 35$ pixels. Bottom panel: $N_{\text{tot}} = 5,000$, $\beta = 0.65$, cavity strength 1.5 (weak cavities) and $D = 35$ pixels. From left to right: Input source model, raw mock image, residual image from the β -fitting method, and the quotient image from unsharp masking (both slightly smoothed).

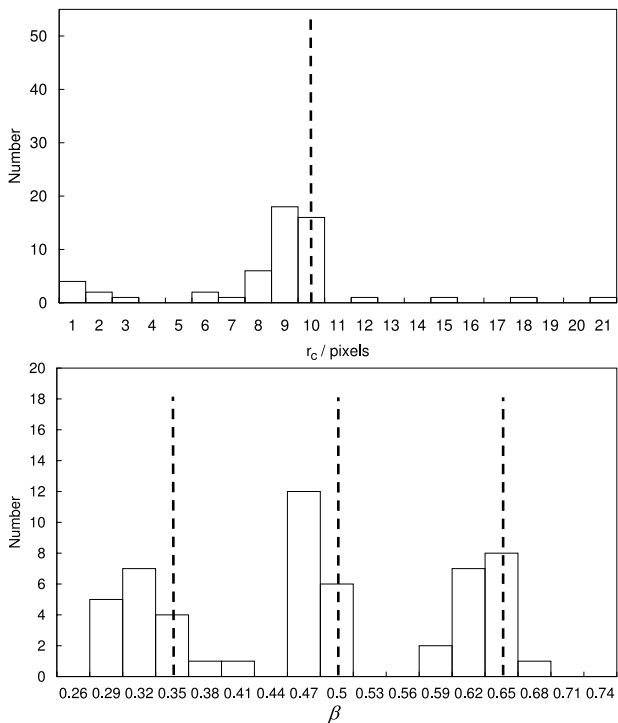


FIG. 12.— Distribution of fit results for (top) core radius r_c and (bottom) β for the mock images. Vertical dashed lines represent the mock input values.

(β , N_{tot} , cavity strength and distance) influence the identification of cavities, even when applying the relatively successful model fitting approach. This is illustrated in Figure 14, which outlines the impact of changing the various model input parameters, again using the classification described in Section 3.3. In particular, the value of N_{tot} emerges as a crucial factor for cavity recovery. Among the 18 mock images with $N_{\text{tot}} = 5,000$, only eight were identified as hosting possible cavities in the residual images, while for $N_{\text{tot}} = 30,000$, the corresponding value is 17 out of 18. Remaining input parameters also play a role. For example, at fixed N_{tot} , cavity recovery is

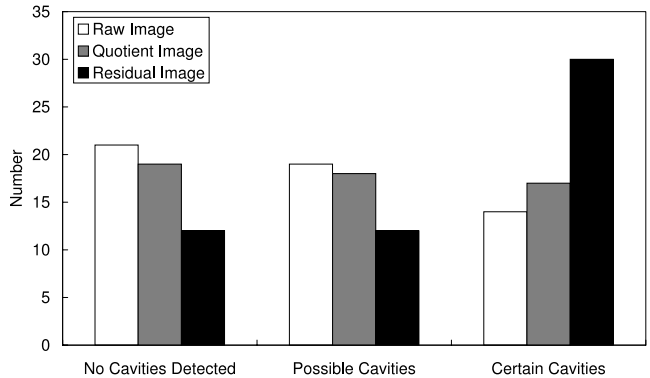


FIG. 13.— Number of mock data sets identified as harboring certain, possible, or no cavities based on the unprocessed mock images (empty bars), quotient images (grey), and on the residual images from model fitting (black).

more efficient for $\beta \geq 0.5$ compared to $\beta = 0.35$, and for higher cavity strength and smaller distance. Another lesson from the mock data was that Poisson noise can easily mask one of the two cavities in X-ray faint sources. In other words, visual identification of only one cavity in unprocessed data does not necessarily exclude the presence of a second cavity. Finally, we note that we found no clear correlation between the identification or input properties of cavities and various statistical moments of the photon number distribution in the residual images.

Naturally, we cannot with confidence exclude the possibility that a few cavities have been falsely identified in the *Chandra* data. This problem necessarily also plagues all other similar studies to some extent, but could be particularly acute for the present work since we have not incorporated radio data or other means to aid in cavity detection. However, we have reasons to believe that this issue is not important within our present analysis. First, as already discussed in Section 4, our comparison to existing results suggests that we have been rather conservative in our cavity identification. Second, none of the identified cavities appears severely discrepant in Figure 8 (note in particular the tightness of the observed correlation between estimated major and minor axis), which argues against a significant population of falsely identified cavities. Third, as mentioned above, within the lowest-S/N mock subsample (featuring 5,000 net counts), we identified cavities in eight out of 18 cases. As can be gleaned from Table 2, the corresponding fraction for all the real data sets with $< 5,000$ counts is comparable but slightly smaller, seven out of 19. This further supports the notion that the incidence of falsely identified cavities in our *Chandra* sample must be small.

5.3. Surface Brightness Modeling versus Unsharp Masking

The two methods considered here for revealing small-scale structure in extended emission each have their strengths and weaknesses. The model-fitting approach clearly requires data of fairly high signal-to-noise ratio to ensure convergence in the fitting process. In addition, it assumes a model for the underlying large-scale emission which may not always provide a good description. With unsharp masking, no assumptions are needed for the large-scale morphology, but the method requires

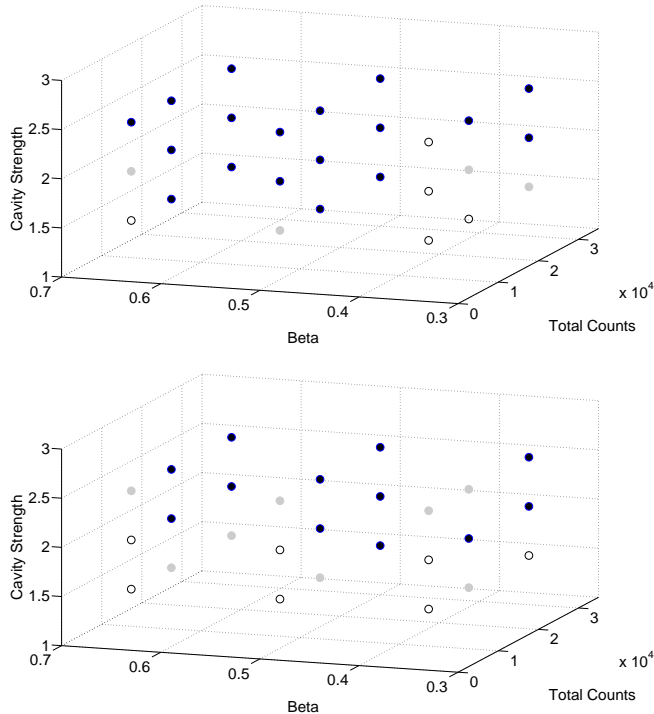


FIG. 14.— Influence of total source counts, β , and cavity strength on cavity recovery in the residual images from β -model fitting. Top panel shows the detection result for the 27 mock simulations with close cavities ($D = 15$ pixels from the group center) and bottom panel the corresponding results for the ones with distant cavities ($D = 35$ pixels). Dark circles represent certain cavity detections, gray circles possible ones, and empty circles data sets with no detectable cavities.

a highly non-trivial choice of smoothing scales. Furthermore, the method normally assumes a circular smoothing kernel, so the smoothing on large scales could potentially generate spurious cavities in systems with a highly elliptical X-ray morphology.

A general conclusion based on all 54 mock images is that the model-fitting method seems superior to unsharp masking in recovering clearly identifiable cavity structures, cf. Figure 13. This is perhaps not surprising, given that the underlying group emission in these data is perfectly described by a β -model (modulo Poisson uncertainties on source and background counts). However, this finding is not limited to our mock data; despite careful consideration of the smoothing scales employed, Figures 4 and Figure 5 show that unsharp masking often produces a lower contrast between the cavities and their surroundings than the output from the model fitting approach. The top panel of Figure 11 further illustrates this point for the mock data, showing another example in which cavities in the residual image are more prominent than those in the quotient image. Another interesting conclusion can be reached from the bottom panel of Figure 11, which emulates a low-S/N data set with only weak cavities. In this case, the two input cavities are reasonably well recovered in the residual image, whereas the quotient image from unsharp masking would lead one to conclude, incorrectly, that cavities are present to the east and west of the center of the group emission. Hence, even in an idealized case such as this, unsharp

masking applied to low-S/N data can produce misleading results. This serves as a cautionary note if using this method alone to search for cavities. Consistency tests using other methods, and/or the inclusion of radio data to support the existence of cavities, may be crucial for reliable identification of cavities in X-ray faint systems.

In addition, the model fitting approach is occasionally able to recover structure that is not seen in the quotient images. For example, in the residual image of A1991 (Figure 4), two cavities are clearly visible, while unsharp masking only hints at the presence of the northern cavity. Nevertheless, unsharp masking can still provide a very useful supplement to visual inspection and surface brightness fitting. This is particularly true in the cases where model fitting clearly fails to converge on sensible parameters (typically in relatively low-S/N data), and for groups in which there are more complicated structures which cannot be described by an elliptical β -model. As seen in Figures 4 and 5, a number of our groups belong to the latter category. For example, IC 1262 presents a sharp surface brightness discontinuity in the central regions, possibly related to a cold front (Trinchieri et al. 2007). NGC 4104 shows a clear depression in central surface brightness, possibly due to cavities being oriented along the line of sight. For RXJ 1159+5531, the fitting approach fails to clearly uncover the two cavities hinted at north-east and south-west of the group center in the unprocessed image. These are located at either end of an X-ray jet, itself situated at the center of the diffuse emission and visible in the raw data (although not clearly so in Figure 5). In the residual image, the cavities are overshadowed by some structure generated in the fitting process as a consequence of the complex morphology in this system. In all these cases, unsharp masking provides valuable aid in cavity identification.

6. DISCUSSION

6.1. Cavity and Central Radio AGN Fractions

In total, we find that 26 out of our 51 groups ($51 \pm 12\%$) show at least tentative evidence for the presence of cavities. While this is statistically inconsistent at the $\sim 4\sigma$ level with *all* our groups showing cavities, our experimentation with mock images suggests that the real fraction might be higher. In particular, since the total number of source counts plays such an important role for the detectability of cavities in our mock data, it is relevant to examine the distribution of total source counts for our real sample. Figure 15 shows the connection between N_{tot} for the observed groups, as defined in Section 4, and our cavity detection results. Groups with $N_{\text{tot}} \geq 10,000$ are very likely to be identified as harboring cavities, while more than two-thirds of the systems with lower N_{tot} show no clear evidence of these. Successful cavity detection is thus clearly biased towards groups with high-S/N data. Despite this, there *are* real (and mock) groups with a large number of counts ($N_{\text{tot}} \geq 30,000$) for which cavities are not detected. In real data, this could certainly be because cavities are absent or present a low intrinsic X-ray contrast, as suggested by our mock results. Alternatively, it may be due to orientation effects, the impact of which we have not tested with the mock data. Also, as discussed above, some of our groups show features which are clearly not well described by a β -model, a fact which

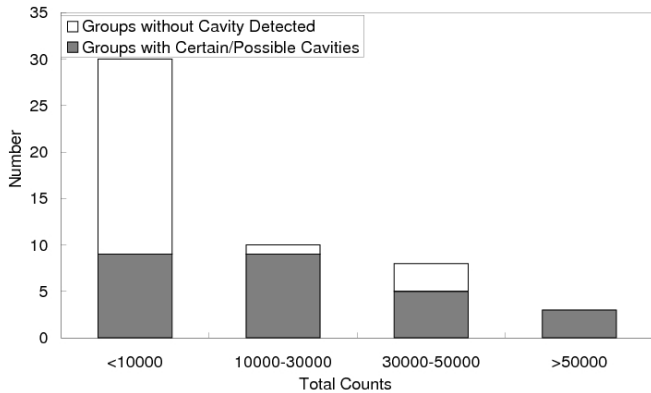


FIG. 15.— Cavity detectability and the distribution of total source counts N_{tot} for all 51 observed groups.

could also complicate cavity recovery when relying on surface brightness modeling in the process.

Nevertheless, given the lower mean S/N of the mock systems with non-detected cavities, our inability to detect cavities in many of the low-S/N *Chandra* data sets may still be consistent with the presence of cavities in these systems. As mentioned, for the lowest-S/N mock subsample, cavities are identified in 8/18 systems, consistent with the 7/19 found in real data. Including brighter systems ($\leq 15,000$ net counts), corresponding values are $19/36 = 53 \pm 15\%$ (mock) and $13/35 = 37 \pm 12\%$ (real), just consistent at $1-\sigma$. The total rate of systems showing evidence of identifiable cavities in the mock data of $42/54$ ($78 \pm 16\%$) is higher than that of the *Chandra* sample however, but the fractions are still consistent at the 90% confidence level. In that sense, our results are broadly consistent with the possibility that most, if not all, of our real groups do harbor cavities. However, we strongly caution against over-interpreting these numbers. Our simplified mock setup was not designed to reproduce the full complexity of the real sample, and the above comparison should be considered indicative at best. Hence, we do not claim our results to suggest that *all* our groups contain cavities, only that the actual fraction is likely considerably higher than the $\sim 50\%$ suggested by our analysis.

A somewhat related question is that of the incidence of central radio AGN within our sample. Since six of our groups are excluded from such considerations due to source confusion or lack of 1.4-GHz coverage, we cannot make statistically robust statements for the full sample. However, among the remaining 45 systems, 34 ($76 \pm 17\%$) host a detectable central radio source. This fraction is higher than the corresponding incidence of detectable cavities ($23/45$, $51 \pm 13\%$), but only marginally so, and it rises to $21/23$ (consistent with 100%) if only considering the groups in the combined C- and P-sample. As such, the fraction of detectable central radio AGN is comparable to that of identifiable cavities, especially considering that the latter is likely a lower limit to the true fraction. We do note that while the N-sample is statistically underrepresented among groups with detectable radio AGN, this is not necessarily the case if adopting a fixed cut in $L_{1.4\text{GHz}}$ so as to focus on radio-loud AGN alone. This is already hinted at in Figure 9, which indicates no

connection between the presence of detectable cavities and the current radio power of the central group galaxy. Furthermore, given that NVSS sensitivity is nearly uniform (Condon et al. 1998) and that the weakest detected radio source within our sample is also the nearest and has a flux just below the NVSS 99% completeness limit, it is clear that all our groups could potentially harbor a central AGN with a 1.4-GHz luminosity brighter than this source ($L_{1.4\text{GHz}} \approx 1 \times 10^{20} \text{ W Hz}^{-1}$).

6.2. Comparison to Results for Clusters

With half of our sample showing some evidence of cavities, our groups are lying between results for individual giant elliptical galaxies ($\sim 1/4$; Nulsen et al. 2009) and the X-ray brightest cool-core clusters ($\sim 2/3$; Dunn & Fabian 2006). Our results in Section 5 suggests that these differences can be at least partly explained by observational biases that favor cavity detection in high-flux systems. In addition, as discussed in Section 4, the surface brightness distribution of groups is generally flatter than in clusters across the relevant radial ranges. The dependence on β of the cavity recovery rate (cf. Figure 14) may therefore also play a role for the above results.

Alternatively, the observed differences in detectable cavity fraction may reflect a more fundamental connection between the presence of high-contrast X-ray cavities and global system properties such as X-ray luminosity or total mass. Under the plausible assumption that X-ray cavities are generated by a radio outburst in the central AGN, the lower cavity fraction in smaller systems could be explained by a systematic variation in central AGN duty cycle with system mass. If X-ray fainter systems generally have shorter central radio outbursts, clearly detectable cavities are perhaps inflated by the AGN in a smaller fraction of those systems. The observed lack of a link between the 1.4 GHz luminosity of any radio source within the central galaxy and the presence of detectable cavities in our sample seems consistent with this possibility. If the outburst phase is relatively short, bright 1.4 GHz emission within the central galaxy may already have subsided when detectable cavities emerge in the intragroup medium. This scenario should be testable with lower-frequency radio data which trace the older, less energetic electron populations from the outburst. Such studies are currently underway (Giacintucci et al. 2009).

With regard to the properties of the detected cavities themselves, another finding of our study is that cavity radii in the radial and tangential directions are highly correlated, with the ratio of the two remaining roughly constant regardless of cavity size. The implication of equations (1)–(3) is that bubbles retain a mean axis ratio of $a/b \sim 1.7$ as they rise and expand in the surrounding medium, until eventually shredded by hydrodynamic instabilities. This finding is in excellent quantitative agreement with results for massive galaxy clusters (Birzan et al. 2004), as illustrated in Figure 8, suggesting that it is a generic feature of cavity evolution regardless of the depth of the local gravitational potential and the entropy gradient of the ambient medium (which set the characteristic buoyancy rise time of the bubbles). Moreover, the tight correlation between the size of the cavity and the projected cavity distance from the group center (as shown in Figure 8) indicates that the apparent

angle opened by the cavity to the center of the group remains nearly constant at $\theta \sim 60^\circ$ during the evolution of the cavity. This is also in remarkable agreement with the case of clusters (Birzan et al. 2004; Diehl et al. 2008), indicating that similar physical processes are responsible for bubble evolution, and their disruption, in systems covering a large range in total mass.

6.3. Implications for the Formation and Evolution of Cavities

It is interesting to note that the gas temperature profiles for our sample (Rasmussen & Ponman 2007; Sun et al. 2009) indicate that 43 of our groups host a cool core, with the eight non-cool core systems all belonging to the N-sample. Hence, the (C- and P-sample) cavity fraction is $60 \pm 15\%$ for cool-core groups, in contrast to the complete absence of identifiable cavities among our non-cool core systems. However, this need not reflect any intrinsic differences between cool-core and non-cool core systems, since cavity detectability is conceivably biased toward cool-core systems with bright central regions (as suggested by Figure 15 and by the increase in cavity recovery rate with both N_{tot} and β for our mock data sets). On the other hand, barring differences in normalization, the surface brightness profiles of our different subsamples show very similar behavior, with comparable mean values of β and r_c . As such, there is no clear evidence that the surface brightness distribution is more centrally peaked for the C- and P-samples, making it worthwhile to briefly discuss whether the different cavity detection rates for cool-core and non-cool core systems reflect a real effect.

While a detailed discussion of the cool core/non-cool core distinction and its possible origins is well beyond the scope of this work, we do note that an increased fraction of detectable cavities among cool-core groups would fit the picture of a self-sustained cooling-driven feedback loop: Strong central cooling of ICM material feeds the supermassive black hole in the central group galaxy, which responds with a radio outburst that creates cavities in the surrounding medium and temporarily re-heats it, until radiative cooling can re-ignite the process. Some support for this comes from the work of Diehl & Statler (2008b), based on a *Chandra* study of 36 ellipticals, ten of which are central group galaxies in our sample (and of which eight show evidence of cavities in the present work). These authors found a relation between the inner radial gas temperature gradient and the central radio AGN power, in the sense that positive (and steeper) inner gradients are preferentially found in optically brighter ellipticals with stronger central radio sources (but see also Fukazawa et al. 2006 and Humphrey et al. 2006). In addition, practically all our groups with identifiable cavities host a detectable central radio source. Although these results suggest a connection between strong central ICM cooling, a powerful AGN radio output, and the presence of detectable cavities, we emphasize that there is still very little *direct* evidence for central gas cooling to low temperatures in groups or clusters. In particular, deep X-ray grating spectroscopy of A262, A3581, and HCG 62, all belonging to our C-sample, has failed to reveal material cooling to below $T \approx 0.5$ keV in their central regions (Sanders et al. 2010). It is also unclear how the central black hole would accomplish the distributed heating

required to completely halt catastrophic cooling at the group core, even if only temporarily. Thus, while the above picture may seem appealing, many of its details still await observational and theoretical verification.

Once formed, the properties of cavities themselves may help to shed light on the processes responsible for their production. In recent years several authors have employed numerical techniques to study the evolution of buoyant bubbles in galaxy groups and clusters, including purely inviscid hydrodynamical simulations in two (Churazov et al. 2001; Brüggén & Kaiser 2002; Reynolds et al. 2002; Brüggén 2003; Sternberg et al. 2007) and three dimensions (Quilis et al. 2001; Basson & Alexander 2003; Omma et al. 2004; Pavlovski et al. 2008; Scannapieco & Brüggén 2008; Brüggén et al. 2009). Results generally show that although under certain circumstances the bubbles could be long-lived, purely hydrodynamical evolution usually cannot prevent bubbles from being rapidly shredded by Rayleigh–Taylor, Kelvin–Helmholtz, or Richtmyer–Meshkov instabilities (e.g., Diehl et al. 2008). To prevent bubble disruption, additional physics such as magnetic fields, thermal conductivity, and viscosity are probably required. With certain geometries, a magnetic field could help to protect the bubble (Brüggén & Kaiser 2001; Robinson et al. 2004; Jones & De Young 2005; Ruszkowski et al. 2007; Liu et al. 2008; Dursi & Pfrommer 2008; O’Neill et al. 2009; Dong & Stone 2009).

Our observation of cavities at projected distances of $D \gtrsim 20$ kpc from the group core implies that bubbles are reasonably resilient to disruption processes, thus confirming the necessity of incorporating such additional physics in numerical work (Jones & De Young 2005). Alternatively, it has been demonstrated that if a bubble is continuously being inflated by a purely hydrodynamical jet (Pizzolato & Soker 2001) or a magnetically dominated jet (Li et al. 2006; Nakamura et al. 2006, 2007), under some circumstances the development of hydrodynamical instabilities could also be suppressed, thus keeping bubbles intact for longer (Diehl & Statler 2007). However, the fact that we find no clear link between the presence of detectable cavities and the current luminosity of any central radio source seems to argue against this mechanism as a general feature in our groups.

To briefly explore the possibility of distinguishing between different model predictions for cavity evolution, we can adopt the approach of Diehl et al. (2008). These authors consider a range of different models for the formation and evolution of cavities, under the reasonable assumptions that the bubbles rise subsonically in the ICM in pressure equilibrium with their surroundings, with the ICM background density described by a β -model. The models considered include one of purely hydrodynamic, adiabatically expanding bubbles containing gas with an adiabatic index $\Gamma = 5/3$ (here denoted “AD53” for consistency with Diehl et al. 2008), and a model in which bubbles are generated by a current-dominated jet (“CDJ”, see, e.g., Li et al. 2006) and have magnetically dominated pressure. In both these models, predicted bubble radii a grow with clustercentric distance D as $a \propto [1 + (D/r_c)^2]^\alpha$, with $\alpha = \beta/(2\Gamma)$ and $\alpha = 3\beta/4$ for the AD53 and CDJ models, respectively. The asymptotic growth of the bubbles (at $D \gg r_c$) is thus a pow-

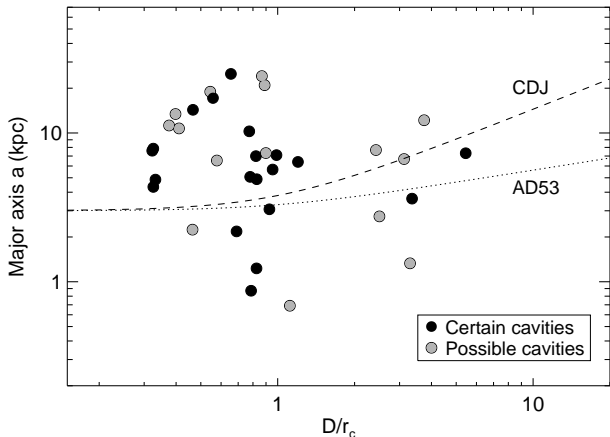


FIG. 16.— Cavity major axis a as a function of projected group-centric distance D normalized by r_c . Dotted line (“AD53”) shows the predicted evolution of a purely hydrodynamical bubble, and dashed line (“CDJ”) that of a magnetically dominated bubble inflated by a current-dominated jet (see text for details), both for an arbitrarily chosen initial bubble size of $a = 3$ kpc.

erful discriminator of these different models. Among the models discussed by Diehl et al. (2008), AD53 represents the slowest and CDJ the fastest expansion of the bubbles. When plotted against D/r_c , Diehl et al. (2008, their figure 2) find that observed cavity sizes at $D \gtrsim 4r_c$ suggest that bubbles expand relatively fast, with CDJ the preferred model.

For comparison, we show a similar plot for our cavity sample in Figure 16. Overplotted are model predictions for the AD53 and CDJ models, both assuming a fixed value of $\beta = 0.45$, the mean value for our groups with detectable cavities. It is clear that we cannot easily distinguish between these two simple models. This is largely due to a dearth of systems with distant cavities in our sample, since — unlike Diehl et al. (2008) — we have only a handful of cavities detected well outside the ICM core radius. A larger group sample, particularly including systems with distant cavities, would be required to make robust statements on the nature of cavities in groups. However, since the cavities within our sample appear to obey the same scaling relations as seen in more massive systems, constraints from studies of cavities in clusters (Diehl et al. 2008) are likely to apply in our groups as well.

7. CONCLUSIONS

Based on *Chandra* archival data of 51 galaxy groups, we have presented the first systematic search for, and analysis of, X-ray cavities in a large sample of groups. At least nine of these groups have previously been reported to show evidence of such cavities. In the present work, the cavities are identified from *Chandra* data alone, either by subtracting an elliptical β -model fit from the X-ray surface brightness distribution, or by performing unsharp masking using two Gaussian smoothing kernels. Based on visual inspection of the resulting images, 13 groups ($\sim 1/4$) within our sample are identified as clearly harboring cavities, and another 13 groups ($\sim 1/4$) show

tentative evidence for cavities. All of these 26 systems show clear evidence for a cool core. The remaining 25 groups have a lower cool-core fraction ($17/25 \approx 70\%$) and do not show convincing evidence for the presence of cavities. The total fraction of groups with some evidence of cavities in our sample is thus 50%, rising to 60% if only considering the cool-core systems. In this respect, our groups are lying between results for individual giant elliptical galaxies ($\sim 1/4$; Nulsen et al. 2009) and cool-core clusters ($\sim 2/3$; Dunn & Fabian 2006). We found no clear link between the current 1.4 GHz radio luminosity of the central brightest group galaxy and the detection of cavities.

To test our ability to identify cavities using the two adopted approaches, we generated a set of mock images designed to mimic typical *Chandra* images of the observed groups. For these data, we find that surface brightness modeling is generally superior to unsharp masking in reliably recovering cavity properties, a conclusion echoing one already hinted at from our analysis of the real data. The results also show that cavity recovery is strongly influenced by a number of factors, including the projected distance between the cavity center and the group center, the significance of the surface brightness depression represented by the cavity, and most importantly, the signal-to-noise ratio of the diffuse group emission. Cavity detectability is highly biased toward X-ray bright systems, implying that the observed cavity fraction in our sample is likely a lower limit.

We find tight correlations between the radial and tangential radii of the cavities in our group sample, and between the size and projected groupcentric distance of cavities. While we are not able to clearly distinguish between simple model predictions for the evolution of cavities on the basis of our sample alone, we note that the observed correlations are in excellent quantitative agreement with results for more massive clusters. This suggests that very similar physical processes are responsible for cavity evolution and disruption in systems covering a large range in mass.

We thank the referee for helpful comments which improved the presentation of our results. This research has made use of data obtained from the Chandra Data Archive and the Chandra Source Catalog, and software provided by the Chandra X-ray Center (CXC) in the application packages CIAO, ChIPS, and Sherpa. This research has also made use of the NASA/IPAC Extragalactic Database (NED) which is operated by the Jet Propulsion Laboratory, California Institute of Technology, under contract with the National Aeronautics and Space Administration. JR acknowledges support provided by the National Aeronautics and Space Administration through Chandra Postdoctoral Fellowship Award Number PF7-80050 issued by the Chandra X-ray Observatory Center, which is operated by the Smithsonian Astrophysical Observatory for and on behalf of the National Aeronautics and Space Administration under contract NAS8-03060. JSM acknowledges partial support for this work from NASA grant NNG04GC846.

REFERENCES

- Becker, R. H., White, R. L., & Helfand, D. J. 1995, *ApJ*, 450, 559
- Benson, A. J., Bower, R. G., Frenk, C. S., Lacey, C. G., Baugh, C. M., & Cole, S. 2003, *ApJ*, 599, 38
- Best, P. N., Kauffmann, G., Heckman, T. M., Brinchmann, J., Charlot, S., Ivezić, Ž., & White, S. D. M. 2005, *MNRAS*, 362, 25
- Best, P. N., Kaiser, C. R., Heckman, T. M., & Kauffmann, G. 2006, *MNRAS*, 368, L67
- Basson, J. F., & Alexander, P. 2003, *MNRAS*, 339, 353
- Birzan, L., Rafferty, D. A., McNamara, B. R., Wise, M. W., Nulsen, P. E. J. 2004, *ApJ*, 607, 800
- Birzan, L., McNamara, B. R., Nulsen, P. E. J., Carilli, C. L., & Wise, M. W. 2008, *ApJ*, 686, 859
- Blanton, E. L., Sarazin, C. L., McNamara, B. R., & Wise, M. W. 2001, *ApJ*, 588, L15
- Bower, R. G., Benson, A. J., Malbon, R., Helly, J. C., Fendk, C. S., Baugh, C. M., Cole, S., & Lacey, C. G. 2006, *MNRAS*, 370, 645
- Brüggen, M. & Kaiser, C. R. 2001, *MNRAS*, 325, 676
- Brüggen, M. & Kaiser, C. R. 2002, *Nature*, 418, 301
- Brüggen, M. 2003, *ApJ*, 592, 839
- Brüggen, M., Scannapieco, E., & Heinz, S. 2009, *MNRAS*, 395, 2210
- Cavaliere, A., & Fusco-Femiano, R. 1976, *A&A*, 49, 137
- Churazov, E., Brügger, M., Kaiser, C. R., Böhringer, H., & Forman, W. 2001, *ApJ*, 554, 261
- Condon, J. J., Cotton, W. D., Greisen, E. W., Yin, Q. F., Perley, R. A., Taylor, G. B., & Broderick, J. J. 1998, *AJ*, 115, 1693
- Croton, D. J., et al. 2006, *MNRAS*, 365, 11
- Diehl, S., & Statler, T. S. 2007, *ApJ*, 668, 150
- Diehl, S., & Statler, T. S. 2008, *ApJ*, 680, 897
- Diehl, S., & Statler, T. S. 2008, *ApJ*, 687, 986
- Diehl, S., Li, H., Fryer, C. L., & Rafferty, D. 2008, *ApJ*, 687, 173
- Dong, R., & Stone, J. M. 2009, *ApJ*, 704, 1309
- Dunn, R. J. H. & Fabian, A. C. 2004, *MNRAS*, 355, 862
- Dunn, R. J. H., Fabian, A. C., & Taylor, G. B. 2005, *MNRAS*, 364, 1343
- Dunn, R. J. H. & Fabian, A. C. 2006, *MNRAS*, 373, 959
- Dursi, L. J. & Pfrommer, C., 2008, *ApJ*, 677, 993
- Enßlin, T. A. & Heinz, S. 2002, *A&A*, 384, L27.
- Fabian, A. C. 1994, *ARA&A*, 32, 277
- Fabian, A. C., Sanders, J. S., Taylor, G. B., Allen, S. W., Crawford, C. S., Johnstone, R. M., & Iwasawa, K. 2006, *MNRAS*, 366, 417
- Fabian, A. C., et al. 2000, *MNRAS*, 318, L65
- Fukazawa, Y., Botoya-Nonesa, J. G., Pu, J., Ohto, A., & Kawano, N. 2006, *ApJ*, 636, 698
- Gastaldello, F., Buote, D. A., Temi, P., Brighenti, F., Mathews, W. G., & Ettori, S. 2009, *ApJ*, 693, 43
- Giacintucci, S., Vrtilik, J. M., O'Sullivan, E., Raychaudhury, S., David, L. P., Venturi, T., Athreya, R., & Gitti, M. 2009, to appear in *AIP Conf. Ser. "The Monster's Fiery Breath: Feedback in Galaxies, Groups, and Clusters"*, Eds. S. Heinz & E. Wilcots (arXiv:0909.0291)
- Humphrey, P. J., Buote, D. A., Gastaldello, F., Zappacosta, L., Bullock, J. S., Brighenti, F., & Mathews, W. G. 2006, *ApJ*, 646, 899
- Isobe, T., Feigelson, E. D., Akritas, M. G., & Babu, G. J. 1990, *ApJ*, 364, 104
- Jethava, N. N., Ponman, T. J., Hardcastle, M. J., & Croston, J. H. 2007, *MNRAS*, 378, 384
- Johnstone, R. M., Allen, S. W., Fabian, A. C., & Sanders, J. S. 2002, *MNRAS*, 298, 854
- Jones, T. W., & De Young D. S. 2005, *ApJ*, 624, 586
- Jones, C., et al., 2002, *ApJ*, 567, L115
- Kaastra, J. S., et al., 2004, *A&A*, 413, 415
- Kraft, R. P., Forman, W. R., Churazov, E., Laslo, N., Jones, C., Markevitch, M., Murray, S. S., & Vikhlinin, A. 2004, *ApJ*, 601, 221
- Li, H., Lapenta, G., Finn, J. M., Li, S., & Colgate, S. A. 2006, *ApJ*, 643, 92
- Liu, W., Li, H., Li, S., & Hsu, S. C. 2008, *ApJ*, 684, L57
- Machacek, M., Nulsen, P. E. J., Jones, C., & Forman, W. R. 2006, *ApJ*, 648, 947
- McNamara, B. R., & Nulsen, P. E. J. 2007, *ARA&A*, 45, 117
- McNamara, B. R., et al. 2000, *ApJ*, 534, L135
- Mohr, J. J., Evrard, A. E., Fabricant, D. G., & Geller, M. J. 1995, *ApJ*, 447, 8
- Mohr, J. J., Mathiesen, B., & Evrard, A. E. 1999, *ApJ*, 517, 627
- Morita, U., Ishisaki, Y., Yamasaki, N. Y., Ota, N., Kawano, N., Fukazawa, Y., & Ohashi, T. 2006, *PASJ*, 58, 719
- Nakamura, M., Li, H., & Li, S. 2006, *ApJ*, 652, 1059
- Nakamura, M., Li, H., & Li, S. 2007, *ApJ*, 656, 721
- Nulsen, P., Jones, C., Forman, W., Churazov, E., McNamara, B., David, L., & Murray, S. 2009, to appear in *AIP Conf. Ser. "The Monster's Fiery Breath: Feedback in Galaxies, Groups, and Clusters"*, Eds. S. Heinz & E. Wilcots (arXiv:0909.1809)
- Omma, H., Binney, J., Bryan, G., & Slyz, A. 2004, *MNRAS*, 348, 1105
- Osmond, J. P. F., & Ponman, T. J. 2004, *MNRAS*, 350, 1511
- O'Neill, S. M., De Young, D. S., & Jones, T. W. 2009, *ApJ*, 694, 1317
- Pavlovski, G., Kaiser, C., R., Pope, E. C. D., & Fangohr, H. 2008, *MNRAS*, 384, 1377
- Peterson, J. R., et al., 2001, *A&A*, 365, L104
- Pizzolato, F., & Soker, N. 2006, *MNRAS*, 371, 1835
- Quilis, V., Bower, R. G., & Balogh, M. L. 2001, *MNRAS*, 328, 1091
- Rafferty, D. A., McNamara, B. R., Nulsen, P. E. J., & Wise, M. W. 2006, *ApJ*, 652, 216
- Rafferty, D. A., McNamara, B. R., & Nulsen, P. E. J. 2008, *ApJ*, 687, 899
- Randall, S. W., Jones, C., Markevitch, M., Blanton, E. L., Nulsen, P. E. J., & Forman, W. R. 2009, *ApJ*, 700, 1404
- Rasmussen, J., & Ponman, T. J. 2007, *MNRAS*, 380, 1554
- Reynolds, C. S., Heinz, S., & Begelman, M. C. 2002, *MNRAS*, 332, 271
- Robinson, K., et al., 2004, *ApJ*, 601, 621
- Russell, P. A., Ponman, T. J., Sanderson, & A. J. R. 2007, *MNRAS*, 378, 1217
- Ruszkowski, M., Enßlin, T. A., Brügger, M., Heinz, S., & Pfrommer, C. 2007, *MNRAS*, 378, 662
- Sanders, J. S., & Fabian, A. C. 2002, *MNRAS*, 331, 273
- Sanders, J. S., & Fabian, A. C. 2007, *MNRAS*, 381, 1381
- Sanders, J. S., Fabian, A. C., Frank, K. A., Peterson, J. R., & Russell, H. R. 2010, *MNRAS*, 402, 127
- Scannapieco, E., & Brügger, M. 2008, *ApJ*, 686, 927
- Sijacki, D., & Springel, V. 2006, *MNRAS*, 366, 397
- Sternberg, A., Pizzolato, F., & Soker, N. 2007, *ApJ*, 656, L5
- Sun, M., Voit, G. M., Donahue, M., Jones, C., Forman, W., & Vikhlinin, A. 2009, *ApJ*, 693, 1142
- Trinchieri, G., Breitschwerdt, D., Pietsch, W., Sulentic, J., & Wolter, A. 2007, *A&A*, 463, 153
- Wise, M. W., McNamara, B. R., Nulsen, P. E. J., Houck, J. C., & David, L. P. 2007, *ApJ*, 659, 1153

TABLE 1
THE GROUP SAMPLE

Group	Obs. ID ^a	Obs. Date (yyyy-mm-dd)	Exposure Time ^b (ks)	Distance ^c (Mpc)
3C 442A	6392	2006-01-12	32.57	105
3C 449	4057	2003-09-18	29.09	66.8
A262	7921	2006-11-20	110.63	64.3
A744	6947	2006-10-22	39.29	321
A1139	9387	2008-03-28	10.05	174
A1177	6940	2006-12-27	33.59	138
A1238	4991	2004-03-28	21.57	324
A1275	6945	2006-20-05	49.32	264
A1692	4990	2004-08-12	21.47	373
A1991	3193	2002-12-16	38.30	255
A2092	9384	2007-11-13	9.99	291
A2462	4159	2002-11-19	39.24	313
A2550	2225	2001-09-03	59.01	546
A2717	6974	2006-04-10	19.79	205
A3581	1650	2001-06-07	7.16	99.9
A3880	5798	2004-12-23	22.20	247
AS1101	1668	2001-08-13	9.95	246
ESO 306-017	3189	2002-03-09	14.05	152
ESO 351-021	5784	2005-04-24	39.46	242
ESO 552-020	3206	2002-10-14	23.62	132
HCG 42	3215	2006-09-08	31.70	60.1
HCG 51	4989	2004-02-15	30.75	113
HCG 62	921	2001-10-09	48.50	61.6
IC 1262	2018	2001-08-23	30.73	137
MKW 4	3234	2002-11-24	29.95	88.5
NGC 383	2147	2000-11-06	44.39	66.7
NGC 507	2882	2006-08-28	43.63	64.5
NGC 533	2880	2002-07-28	37.58	72.8
NGC 741	2223	2001-01-28	30.32	73.4
NGC 1132	3576	2003-11-16	39.58	93.8
NGC 1407	791	2007-06-05	48.45	22.8
NGC 1550	5800	2005-10-22	44.37	50.2
NGC 2300	4968	2006-05-24	45.57	25.8
NGC 3402	3243	2002-11-05	29.51	68.7
NGC 4104	6939	2006-02-16	35.82	123
NGC 4125	2071	2007-01-04	64.22	20.2
NGC 4325	3232	2003-02-04	30.07	113
NGC 5044	9399	2008-03-09	82.65	41.7
NGC 5098	6941	2005-11-01	38.53	164
NGC 5129	7325	2006-05-14	25.78	100
NGC 5846	7923	2007-06-14	90.00	26.2
NGC 6269	4972	2003-12-29	39.58	147
NGC 6338	4194	2003-09-17	47.33	115
NGC 7619	3955	2006-07-05	36.75	46.9
RBS 461	4182	2003-03-11	23.45	120
RXJ 1022+3830	6942	2006-10-14	41.43	213
RXJ 1159+5531	4964	2004-02-11	75.06	356
RXJ 1206-0744	9388	2007-11-15	9.99	295
UGC 842	4963	2005-02-13	39.24	188
UGC 2755	2189	2001-02-07	15.62	100
UGC 5088	3227	2002-03-10	34.32	117

^a *Chandra* Observation ID.

^b Cleaned *Chandra* exposure time.

^c Luminosity distance from the NASA/IPAC Extragalactic Database (NED), in the reference frame defined by the cosmic microwave background.

TABLE 2
 FIT RESULTS AND CAVITY PROPERTIES

Group	Cavity ^a	r_c (kpc)	β	D^b (kpc)	a^c (kpc)	b^d (kpc)	N_{tot}^e	$\log L_{1.4\text{GHz}}^f$ (W Hz ⁻¹)
A262	C	6.94 ^{+0.06} _{-0.06}	0.417 ^{+0.001} _{-0.001}	5.7 5.4	4.9 5.1	3.3 3.1	190240	22.51
A1991	C	18.57 ^{+0.15} _{-0.15}	0.458 ^{+0.001} _{-0.001}	10.4 12.2	17.2 24.9	13.1 9.9	59248	23.48
A3581	C	9.52 ^{+0.29} _{-0.28}	0.380 ^{+0.003} _{-0.003}	3.1 3.1	7.9 4.3	3.8 3.7	17932	23.89
A3880	C	15.75 ^{+0.33} _{-0.33}	0.423 ^{+0.002} _{-0.002}	12.2	10.3	8.2	12693	...
HCG 62	C	6.50 ^{+0.06} _{-0.06}	0.483 ^{+0.002} _{-0.002}	5.3 7.8	7.0 6.4	4.1 4.4	45614	21.35
IC 1262	C	20.83 ^{+0.36} _{-0.36}	0.407 ^{+0.002} _{-0.002}	9.7	14.3	10.0	35068	22.56
NGC 533	C	1.72 ^{+0.03} _{-0.03}	0.490 ^{+0.003} _{-0.003}	1.2 1.6	2.2 3.1	1.3 1.6	14851	22.26
NGC 1132	C	0.71 ^{+0.03} _{-0.03}	0.436 ^{+0.004} _{-0.004}	3.9	7.3	3.3	12131	21.75
NGC 4104	C	1.99 ^{+0.05} _{-0.05}	0.632 ^{+0.009} _{-0.009}	0.0 ^g	1.9	1.5	4916	21.96
NGC 5044	C	14.79 ^{+0.07} _{-0.07}	0.480 ^{+0.001} _{-0.001}	4.8 4.9	7.6 4.9	4.7 3.5	329715	21.90
NGC 5098	C	1.18 ^{+0.05} _{-0.05}	0.369 ^{+0.003} _{-0.003}	4.0	3.6	2.3	11807	23.60
NGC 5846	C	0.76 ^{+0.01} _{-0.01}	0.396 ^{+0.001} _{-0.001}	0.6 0.6	1.2 0.9	0.8 0.6	42072	21.23
NGC 6338	C	3.25 ^{+0.99} _{-3.25}	0.470 ^{+0.038} _{-0.156}	3.1 3.2	5.7 7.1	3.1 2.9	15596	22.84
3C 442A	P			9.8 8.9	6.8 5.7	3.8 3.7	2456	24.64
A2550	P	18.94 ^{+0.29} _{-0.28}	0.446 ^{+0.002} _{-0.002}	10.3 7.8	18.9 10.7	9.3 5.9	14834	...
A2717	P	20.98 ⁺¹ _{-0.97}	0.363 ^{+0.005} _{-0.005}	7.9 8.4	11.2 13.4	6.3 5.8	7443	24.41
AS1101	P	60.94 ^{+0.28} _{-0.28}	0.570 ^{+0.003} _{-0.003}	24.2 23.6	21.0 24.1	14.7 15.7	40594	...
ESO 351-021	P	3.96 ^{+0.13} _{-0.12}	0.516 ^{+0.006} _{-0.006}	14.8	12.2	8.6	4756	22.72
NGC 507	P			7.2	6.4	4.1	19787	22.69
NGC 741	P	0.60 ^{+0.02} _{-0.02}	0.467 ^{+0.004} _{-0.004}	1.5	2.8	1.7	4388	23.84
NGC 1407	P	0.29 ^{+0.01} _{-0.01}	0.392 ^{+0.003} _{-0.003}	0.3	0.7	0.4	16126	21.74
NGC 1550	P	3.13 ^{+0.05} _{-0.05}	0.386 ^{+0.002} _{-0.002}	1.5	2.2	1.2	49021	21.70
NGC 2300	P	0.44 ^{+0.02} _{-0.02}	0.457 ^{+0.005} _{-0.005}	1.5	1.3	1.0	4234	20.36
RXJ 1159+5531	P	3.10 ^{+0.06} _{-0.06}	0.526 ^{+0.004} _{-0.003}	7.5 9.7	7.7 6.7	3.9 4.3	8128	< 22.71
RXJ 1206-0744	P			29.1	27.6	21.4	949	< 22.55
UGC 5088	P	9.35 ^{+0.9} _{-0.85}	0.481 ^{+0.028} _{-0.025}	8.4 5.4	7.3 6.5	5.4 3.6	2097	21.08
3C 449	N	0.39 ^{+0.03} _{-0.03}	0.550 ^{+0.018} _{-0.016}				1764	24.29
A744	N	29.83 ^{+1.3} _{-1.27}	0.372 ^{+0.004} _{-0.004}				5260	< 22.62
A1139	N						1948	< 22.09
A1177	N	0.97 ^{+0.09} _{-0.08}	0.662 ^{+0.042} _{-0.035}				3819	< 21.89
A1238	N						1395	...
A1275	N	30.20 ^{+0.99} _{-0.97}	0.404 ^{+0.004} _{-0.004}				7811	< 22.45
A1692	N						1543	...
A2092	N						789	< 22.54
A2462	N						10261	25.24
ESO306-017	N	1.12 ^{+0.07} _{-0.07}	0.421 ^{+0.006} _{-0.006}				5718	...
ESO552-020	N	0.51 ^{+0.05} _{-0.04}	0.375 ^{+0.005} _{-0.005}				5414	< 21.85
HCG42	N	3.54 ^{+0.25} _{-0.05}	0.425 ^{+0.009} _{-0.002}				7297	22.02
HCG 51	N	0.48 ^{+0.03} _{-0.03}	0.478 ^{+0.008} _{-0.008}				3335	< 21.73
MKW 4	N	5.37 ^{+0.07} _{-0.07}	0.447 ^{+0.002} _{-0.002}				32765	22.21
NGC 383	N	1.01 ^{+0.04} _{-0.04}	0.666 ^{+0.015} _{-0.014}				2888	24.41
NGC 3402	N	2.30 ^{+0.03} _{-0.03}	0.424 ^{+0.001} _{-0.001}				39972	21.67
NGC 4125	N	0.15 ^{+0.01} _{-0.01}	0.373 ^{+0.003} _{-0.003}				8878	19.95
NGC 4325	N	23.21 ^{+0.21} _{-0.21}	0.624 ^{+0.003} _{-0.003}				39165	< 21.71
NGC 5129	N	0.93 ^{+0.05} _{-0.04}	0.498 ^{+0.009} _{-0.009}				2592	21.93
NGC 6269	N	1.09 ^{+0.06} _{-0.06}	0.534 ^{+0.011} _{-0.011}				2843	23.11
NGC 7619	N	0.41 ^{+0.01} _{-0.01}	0.456 ^{+0.003} _{-0.003}				6666	21.73
RBS 461	N						8079	22.54
RXJ 1022+3830	N	14.23 ^{+0.67} _{-0.66}	0.342 ^{+0.004} _{-0.004}				6896	< 22.26

TABLE 2
FIT RESULTS AND CAVITY PROPERTIES

UGC 842	N			3592	22.23
UGC 2755	N	$0.60^{+0.08}_{-0.60}$	$0.679^{+0.098}_{-0.181}$	408	24.24

^a Classification according to whether the group contains certain cavities (C), possible cavities (P), or no detectable cavities (N).

^b Projected distance from cavity center to the X-ray center of the group.

^c Cavity size in tangential direction (projected major axis a defined in Section 3.3).

^d Cavity size in radial direction (projected minor axis b defined in Section 3.3).

^e Number of 0.3–2 keV photons from diffuse emission on the central CCD.

^f Radio luminosity at 1.4 GHz of any radio source within the central brightest group galaxy, extracted from the NRAO VLA Sky Survey (NVSS; Condon et al. 1998). See text for details.

^g The cavity in NGC 4104 is at the very center of the X-ray emission.